

A slice classification neural network for automated classification of axial PET/CT slices from a multi-centric lymphoma dataset

Shadab Ahamed^{1,2,3}, Yixi Xu³, Ingrid Bloise⁵, Joo H. O⁴, Carlos F. Uribe^{2,5,6}, Rahul Dodhia³, Juan L. Ferres³, and Arman Rahmim^{1,2,6}

¹Department of Physics & Astronomy, University of British Columbia, Vancouver, BC, Canada

²Department of Integrative Oncology, BC Cancer Research Institute, Vancouver, BC, Canada

³AI for Good Lab, Microsoft, Redmond, WA, USA

⁴Seoul St. Mary's Hospital, The Catholic University of Korea, Seoul, Republic of Korea

⁵BC Cancer, Vancouver, BC, Canada

⁶Department of Radiology, University of British Columbia, Vancouver, BC, Canada

ABSTRACT

Automated slice classification is clinically relevant since it can be incorporated into medical image segmentation workflows as a preprocessing step that would flag slices with a higher probability of containing tumors, thereby directing physicians' attention to the important slices. In this work, we train a ResNet-18 network to classify axial slices of lymphoma PET/CT images (collected from two institutions) depending on whether the slice intercepted a tumor (positive slice) in the 3D image or if the slice did not (negative slice). Various instances of the network were trained on 2D axial datasets created in different ways: (i) slice-level split and (ii) patient-level split; inputs of different types were used: (i) only PET slices and (ii) concatenated PET and CT slices; and different training strategies were employed: (i) center-aware (CAW) and (ii) center-agnostic (CAG). Model performances were compared using the area under the receiver operating characteristic curve (AUROC) and the area under the precision-recall curve (AUPRC), and various binary classification metrics. We observe and describe a performance overestimation in the case of slice-level split as compared to the patient-level split training. The model trained using patient-level split data with the network input containing only PET slices in the CAG training regime was the best performing/generalizing model on a majority of metrics. Our models were additionally more closely compared using the sensitivity metric on the positive slices from their respective test sets.

Keywords: Lymphoma, ¹⁸F-FDG PET/CT, binary classification, ResNet-18, Focal loss, center-aware training, center-agnostic training, SUV_{max}.

1. INTRODUCTION

¹⁸F-Fluorodeoxyglucose positron emission tomography/computed tomography (¹⁸F-FDG PET/CT) is the current standard of care for imaging lymphoma. Accurate detection and segmentation of lymphoma tumors from PET/CT images have important implications for treatment planning such as radiotherapy and surgical interventions.¹⁻³ Tumor segmentation is also required for the quantification of the total metabolic tumor volume (TMTV) - a metric that has predictive value for patient outcomes in lymphoma.⁴⁻⁷ Manual segmentation of tumors from whole-body PET/CT images is time-consuming and operator-dependent; hence it is not performed routinely.^{8,9} In recent years, the use of deep learning methods has been increasing rapidly in the medical image analysis domain, which can be employed to automate some of these manual tasks.¹⁰⁻¹⁵

Automated slice classification has clinical value since it can be incorporated into medical image segmentation workflows as a preprocessing step that would flag the slices with a higher probability of containing tumors,

Further author information: (Send correspondence to S. A.)

S. A.: E-mail: shadabahamed1996@gmail.com

thereby directing the physician’s attention to the important slices. Our previous work³ performed a classification of axial PET slices into slices containing tumors (positive slices) vs. slices not containing any tumor (negative slices) as a preprocessing step for downstream tasks of tumor localization and segmentation. It demonstrated that an a priori rejection of negative slices was crucial for training the tumor detection and segmentation models since then these modules can be trained on only the positive slices. This made it easier for the detection and segmentation modules to learn contextual representations from the positive slices without being distracted by the noise brought in by the negative examples in the training process.

In this work, we implemented, trained, and validated an automated slice classification network. In contrast to the network in our previous work³ that was trained on a smaller uni-centric dataset, this network was trained on a considerably larger and enriched dataset collected at two different institutions (in Canada and South Korea). We trained various models on different types of train-test splits of these datasets, compared their performances using two metrics (i) area under the receiver operating characteristic curve (AUROC), and (ii) area under the precision-recall curve (AUPRC), and discussed ways to improve model generalization, especially to the external cohort. In the end, we evaluate the binary classification metrics for the models based on a specific training methodology and discuss their ability to correctly classify the positive slices.

2. METHODS

2.1 Dataset

The lymphoma PET/CT dataset consisted of images collected at two institutions: BC Cancer, Vancouver, Canada (BCCV) ($n = 246$; mean age, 49 years; age range, 19-89 years; 129 females), and St. Mary’s Hospital, Seoul, South Korea (SMHS) ($n = 220$; mean age, 59 years; age range, 14-87 years; 103 females)*. The lymphoma tumors in both these datasets were collectively annotated by 4 nuclear medicine (NM) physicians at BCCV and 1 NM physician at SMHS. The physicians manually annotated each of the tumor volumes on the PET images using the PETEdge tool from MIM (MIM Software, Cleveland, Ohio). Note that out of the $n = 246$ images from BCCV, only 10 images were collectively annotated by 4 physicians, while the rest were annotated by only one physician (who was one among the four). For those 10 cases, the final ground truth was generated from the individual physician’s annotations using the Simultaneous Truth and Performance Level Estimation (STAPLE) algorithm.¹⁶

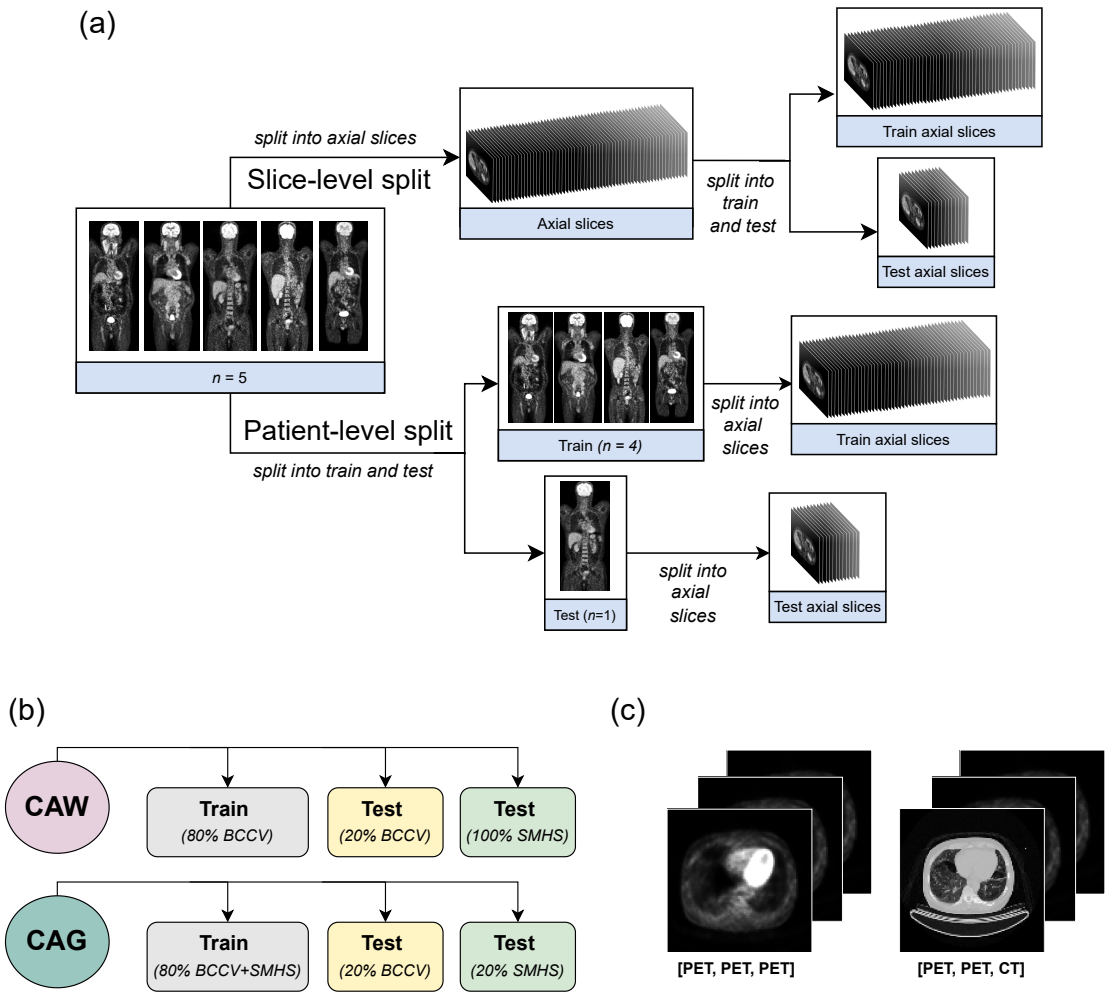
The class imbalance between positive and negative axial slices was 8:92 % and 21:79 % in the BCCV and SMHS sets, respectively. The higher proportion of positive slices in the SMHS set is due to a larger average number of 3D tumors per patient (N) (mean $N = 11$, range=[1, 128]) and TMTV (mean TMTV = 488.43 ml, range = [1.09, 5919.45] ml), as compared to the BCCV set (mean $N = 3$, range = [1, 82]) and mean TMTV = 119.25 ml, range = [0.26, 1416.26] ml). A detailed description of the number of axial slices used in various experiments is given in Table 1

2.2 Image preprocessing

Our models were trained on the axial slices of 3D whole-body images. The 3D PET images (attenuation-corrected) were converted into units of SUV_{bw} and the CT images were in Hounsfield Units (HU). All the CT images were resampled to have the same size and voxel spacing as PET images. The CT images were also denoised via median filtering with a window size of $5 \times 5 \times 5$ that removed the CT intensity outliers (very large HU values $\gtrsim 2000$) while preserving the edges. The proposed network (see next subsection) required a 3-channel input image of size 224×224 . All the PET and CT slices were resized to 224×224 pixels. The inputs were created to have 3-channels because that was a requirement imposed by the network (as it contained fully-connected layers). Two types of inputs were created for our various experiments in this work: (1) Using only PET slices: input = [*PET slice*, *PET slice*, *PET slice*], and (2) Using both PET and CT slices: input = [*PET slice*, *PET*

*Both these datasets are not publicly available and would require BC Cancer Research Ethics Board (UBC BC Cancer REB) approval for access.

slice, CT slice]. Hence, each input was created by stacking the same axial 2D 1-channel PET slice thrice (as in (1)), or by stacking the same PET slice twice and using the corresponding CT slice as the third channel (as in (2)). The maximum PET intensity value of the tumors in the two datasets was $SUV_{bw, \max \text{ tumor}} \approx 48$, so any PET pixel with $SUV_{bw} > 50$ was set to 50, to improve the signal coming from the tumors in the presence of other high(er)-uptake regions such as the brain or bladder. Similarly, the intensities of CT slices were clipped between $[-1024, 1024]$ HU to remove the contribution from bones, calcium, and metal (these have $HU > 1000^{17}$). In the next step, the PET and CT slices were normalized to values between (0, 1) using $PET_{norm} = PET/50$ and $CT_{norm} = (CT + 1024)/2048$, respectively before inputting them into the network. Each input slice was labeled as ‘0’ (negative slice) or ‘1’ (positive slice) with the help of the physicians’ annotations.



2.3 Data splitting for model generalization

The models were trained on two different types of train-test splits of the data. These are explained as follows:

1. **Slice-level split:** The 3D images were first split into individual axial slices and then these slices were split 80:20 % into train and test sets, respectively. Models trained on this kind of data are denoted as M^S .
2. **Patient-level split:** The 3D images were first split 80:20 % into train and test sets, and then were split into individual axial slices. Models trained on this kind of data are denoted as M^P .

For each of the two cases above, two types of models were trained and tested:

1. **Center-aware (CAW) training:** In this case, the model was trained on 80% of BCCV data, and tested on the internal and external test sets, namely the remaining 20% of BCCV data and 100% of SMHS data (external cohort). Models trained in this way are denoted as M_{CAW} .
2. **Center-agnostic (CAG) training:** The model was trained on 80% of combined BCCV+SMHS data and tested on the remaining 20% of BCCV and 20% of SMHS data. Models trained in this way are denoted as M_{CAG} .

During training, the training data in each case was further split into training and validation sets (80:20 %), and the model with the lowest loss on the validation set was chosen as the optimal model for testing.

Split-type (CAW)	Training + Validation set (80% BCCV)	Internal cohort test set (20% BCCV)	External cohort test set (100% SMHS)
Slice-level split	50067	12515	79530
Patient-level split	50479	12103	79530

Split-type (CAG)	Training + Validation set (80% BCCV+SMHS)	Test set (20% BCCV)	Test set (20% SMHS)
Slice-level split	113692	12515	15905
Patient-level split	114503	12103	15506

Table 1. Table showing a description of the number of axial slices in Training + Validation and test sets for slice-level and patient-level split for the CAW (above) and CAG (below) training strategies. During training, the Training + Validation was further split into training and validation sets (80:20 %).

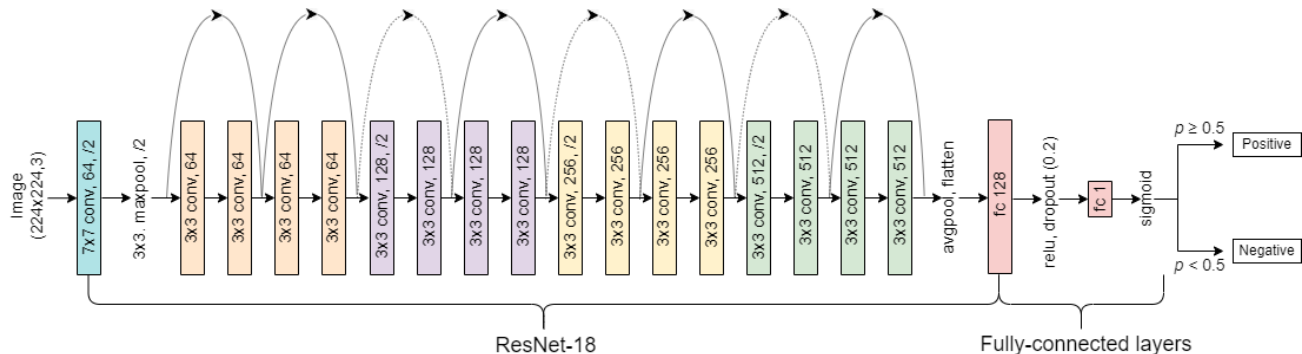


Figure 2. Proposed binary classification network with an ImageNet-pretrained ResNet-18¹⁸ module followed by fully-connected layers.

2.4 Network architecture and training

We implemented a binary classification network with an ImageNet-pretrained ResNet-18¹⁸ backbone followed by fully-connected layers ending in a sigmoid, producing an output $p \in (0, 1)$ (see Figure 2). A slice was classified as a positive slice if $p \geq 0.5$, or as a negative slice if $p < 0.5$. The model’s weights were optimized using the Adam optimizer with a constant learning rate= 10^{-3} . The gradients of the weights of the pretrained ResNet-18 were not frozen and the entire network was fine-tuned during training. Focal loss with hyperparameters $\alpha = 0.25$ and $\gamma = 2$ was used to enhance the binary classification performance in the presence of extreme class imbalance between the positive and negative slices.¹⁹

3. RESULTS

3.1 Model performance

The performance of the various trained models was compared based on the AUROC and AUPRC values obtained on their respective test sets as shown in Table 2. While we report both AUROC and AUPRC in our results, we emphasize that for our datasets with a large class imbalance between the positive and negative slices, the AUPRC metric is more important than AUROC (it is more appropriate to draw performance-based conclusions from the ROC curve when the classes are balanced and from the PRC when the classes are imbalanced).

Several interesting conclusions can be drawn from the metrics shown in the table above. Firstly, let’s compare the two cases where the input = [*PET slice*, *PET slice*, *PET slice*]. The CAW model trained on slice-level split data (M_{CAW}^S (20% BCCV): AUROC=0.99, AUPRC=0.96) outperformed the corresponding CAW model trained on patient-level split data (M_{CAW}^P (20% BCCV): AUROC=0.89, AUPRC=0.70) on the 20% BCCV test set (internal test set) by a large margin. This drop in performance can be attributed to the manner the dataset was split into train-test sets in the two cases. For the slice-level split case, different slices from the same patient can exist in training and test sets, making the model memorize the contextual information from a patient in the training set and predict the class correctly with a high probability whenever another nearby slice from the same patient happens to be in the test set, leading to an overestimation of the classification performance.

Slice-level split						Patient-level split											
Input = [PET, PET, PET]						Input = [PET, PET, PET]						Input = [PET, PET, CT]					
M_{CAW}^S			M_{CAG}^S			M_{CAW}^P			M_{CAG}^P			M_{CAW}^P			M_{CAG}^P		
Test set	AU ROC	AU PRC	Test set	AU ROC	AU PRC	Test set	AU ROC	AU PRC	Test set	AU ROC	AU PRC	Test set	AU ROC	AU PRC	Test set	AU ROC	AU PRC
20% BCCV	0.99	0.96	20% BCCV	0.99	0.97	20% BCCV	0.89	0.70	20% BCCV	0.91	0.71	20% BCCV	0.90	0.70	20% BCCV	0.91	0.71
100% SMHS	0.81	0.63	20% SMHS	0.99	0.98	100% SMHS	0.86	0.71	20% SMHS	0.92	0.85	100% SMHS	0.83	0.68	20% SMHS	0.91	0.86

Table 2. Table showing the performance of various trained classification models on their various test sets using AUROC and AUPRC metrics. The models M_{CAW}^S and M_{CAW}^P have been tested on 20% BCCV (internal cohort) and 100% SMHS (external cohort), while the models M_{CAG}^S and M_{CAG}^P have been test on 20% BCCV and 20% SMHS test sets. On the slice-level data, the models overestimate the performance since the training and test datasets are not independent. The performance of the M_{CAG} models was always better than their respective M_{CAW} models showing that the datasets from the two institutions were quite different and it was important to include slices from SMHS to the training set to make the models generalize better. We also noted that using CT information provided practically no gain in classification performance (and also deteriorated the performance by a few percentages on some of the metrics).

On the other hand, in the patient-level split case, the training and test sets are totally independent of each other at the patient level. A similar conclusion can be drawn when comparing the CAG models where the models trained on slice-level split data ($(M_{CAG}^S$ (20% BCCV): AUROC=0.99, AUPRC=0.97) and (M_{CAG}^S (20% SMHS): AUROC=0.99, AUPRC=0.98)) outperformed those trained on the patient-level split data ($(M_{CAG}^P$ (20% BCCV): AUROC=0.91, AUPRC=0.71) and (M_{CAG}^P (20% SMHS): AUROC=0.92, AUPRC=0.85)). Hence, our results suggest that when training 2D models, one must perform a patient-level split of their data to prevent

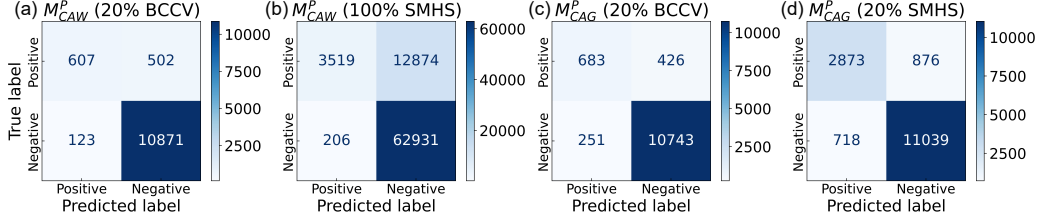


Figure 3. Confusion matrices for the models (a) M_{CAW}^P (20% BCCV), (b) M_{CAW}^P (100% SMHS), (c) M_{CAG}^P (20% BCCV), and (d) M_{CAG}^P (20% SMHS), evaluated on their respective test sets (given in brackets).

performance overestimation.

It is also interesting to note that despite this drop in performance for the CAW model on the internal test cohort when going from slice-level split to patient-level split data, the CAW model trained on patient-level split data (M_{CAW}^P (100% SMHS): AUROC=0.86, AUPRC=0.71) generalized better than the CAW model trained on slice-level split data (M_{CAW}^S (100% SMHS): AUROC=0.81, AUPRC=0.63) on the 100% SMHS test set (external cohort).

Secondly, we also trained models on the patient-level split data with input = [*PET slice*, *PET slice*, *CT slice*] so as to utilize the anatomical information from the CT slices. There wasn't much difference in the performance metrics upon replacing a PET slice with a CT slice as one of the channels, except for M_{CAW}^P (100% SMHS) where there was a drop of 3% in both AUROC and AUPRC for external validation upon including CT. These findings can be explained in one of the following ways: (a) the replacement of the PET slice with a CT slice in the 3-channel image reduced the overall signal in the image from the tumor/background on the positive/negative slices; (b) the clipping of CT slice intensities in the range [-1024, 1024] HU might not be an optimal preprocessing for this problem, and other preprocessing methods must be investigated; (c) the current dataset is not large enough to efficiently utilize the anatomical information from the CT images.

It can also be concluded that the models trained on just the 80% BCCV data (M_{CAW}^S and M_{CAW}^P) do not generalize well to the SMHS data, and hence including SMHS data in the training process is crucial for model generalization as it can be seen from the higher classification performances of M_{CAG}^S and M_{CAG}^P on 20% SMHS data as compared to the that of M_{CAW}^S and M_{CAW}^P on 100% SMHS data (external test cohort).

3.2 Classification metrics

The models trained on patient-level split data (M_{CAW}^P and M_{CAG}^P) with inputs as [*PET slice*, *PET slice*, *PET slice*] were evaluated with binary classification metrics such as sensitivity, specificity, precision, negative predictive value (NPV), accuracy, balanced accuracy, and F1 score. The confusion matrices for the cases M_{CAW}^P (20% BCCV), M_{CAW}^P (100% SMHS), M_{CAG}^P (20% BCCV), and M_{CAG}^P (20% SMHS) are given in Figures 3(a), 3(b), 3(c), and 3(d), respectively. The classification metrics were computed at the test set level in Figure 4(a) and at the patient level within the test sets in Figure 4(b). It can be seen that the performances of M_{CAW}^P (20% BCCV) and M_{CAG}^P (20% BCCV) are nearly the same for all metrics, while the M_{CAG}^P (20% SMHS) in general outperforms M_{CAW}^P (100% SMHS) on most metrics (except for specificity and precision). This is because M_{CAW}^P was trained only on the 80% BCCV set, it failed to learn representative features of the SMHS set, while M_{CAG}^P being trained on a combination of BCCV and SMHS sets was good at predicting the correct class for the slices from both the institutions. This could be attributed to a number of large variabilities between the dataset from the two centers such as differences in average TMTV and the average number of tumors per patient. Interestingly, our network architecture and training methodology leads to a very low number of false positive predictions, resulting in considerably high specificity values (> 0.95) at both the test set and patient level for all the models.

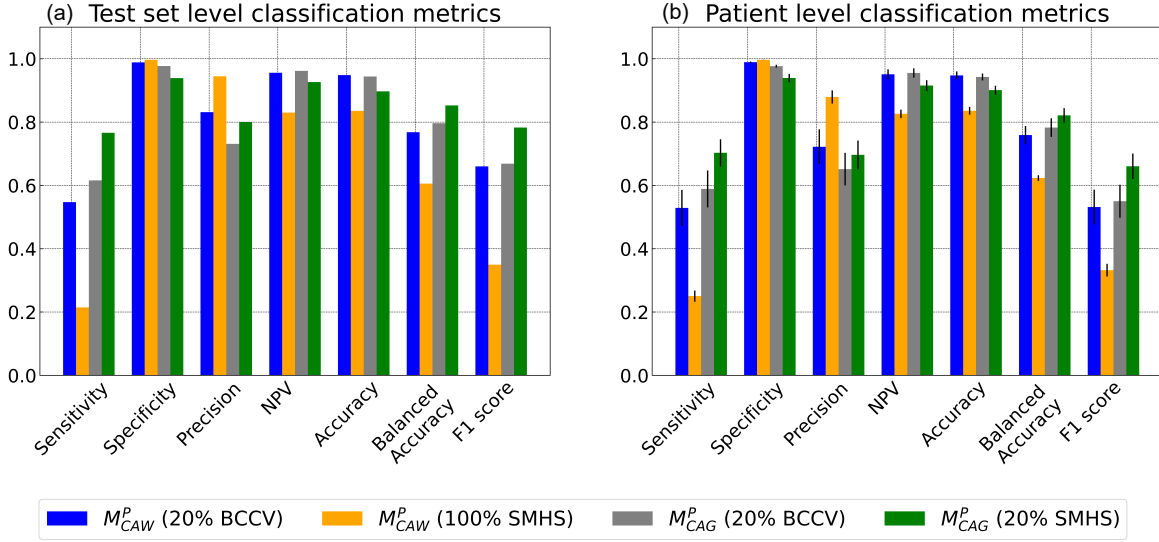


Figure 4. Evaluation of trained binary classifiers M_{CAW}^P (20% BCCV), M_{CAW}^P (100% SMHS), M_{CAG}^P (20% BCCV), and M_{CAG}^P (20% SMHS) on their respective test sets (given in brackets). Classification metrics were evaluated at the test set level (a) and at the patient level (b) within these test sets.

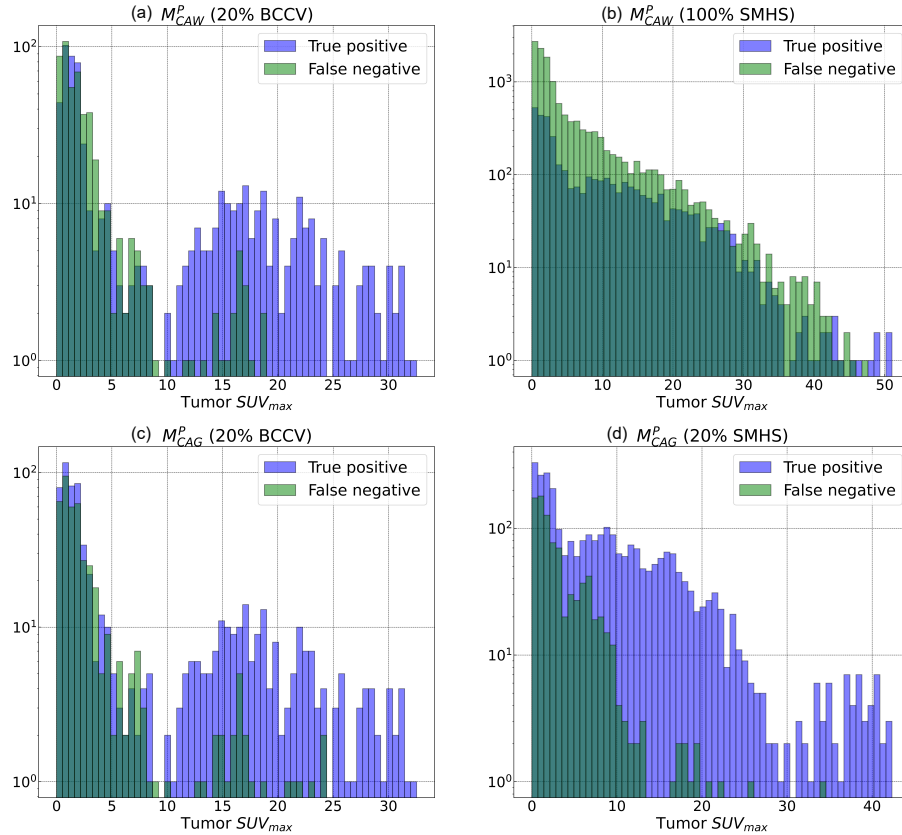


Figure 5. The histograms show the distribution of the number of true positive and false negative predictions as a function of tumor SUV_{max} for (a) M_{CAW}^P (20% BCCV), (b) M_{CAW}^P (100% SMHS), (c) M_{CAG}^P (20% BCCV), and (d) M_{CAG}^P (20% SMHS) on their respective test sets (given in brackets).

3.3 Assessing the classification performance for positive slices (sensitivity analysis)

The classification performance was more closely investigated for the positive slices. The SUV_{\max} values of the tumors on the positive slices were noted and its dependence on the model's classification performance (into true positive or false negative) was evaluated for the cases M_{CAW}^P (20% BCCV), M_{CAW}^P (100% SMHS), M_{CAG}^P (20% BCCV), and M_{CAG}^P (20% SMHS) as shown in the histograms in Figures 5(a), 5(b), 5(c), and 5(d), respectively. The histograms for M_{CAW}^P (20% BCCV), M_{CAG}^P (20% BCCV), and M_{CAG}^P (20% SMHS) show that a larger number of positive slices were classified correctly that had larger values of tumor SUV_{\max} , while there was a similar proportion of true positives and false negatives for slices with lower SUV_{\max} . We hypothesize that the correct classification of some of the slices with low SUV_{\max} is due to the fact that these slices intercepted a larger portion of the 3D tumor (ongoing efforts). On the contrary, the histogram for M_{CAW}^P (100% SMHS) shows that in this case most of the positive slices were classified as false negatives, which is also the reason for the considerably low sensitivity for M_{CAW}^P (100% SMHS) as compared to M_{CAW}^P (20% BCCV), M_{CAG}^P (20% BCCV), and M_{CAG}^P (20% SMHS).

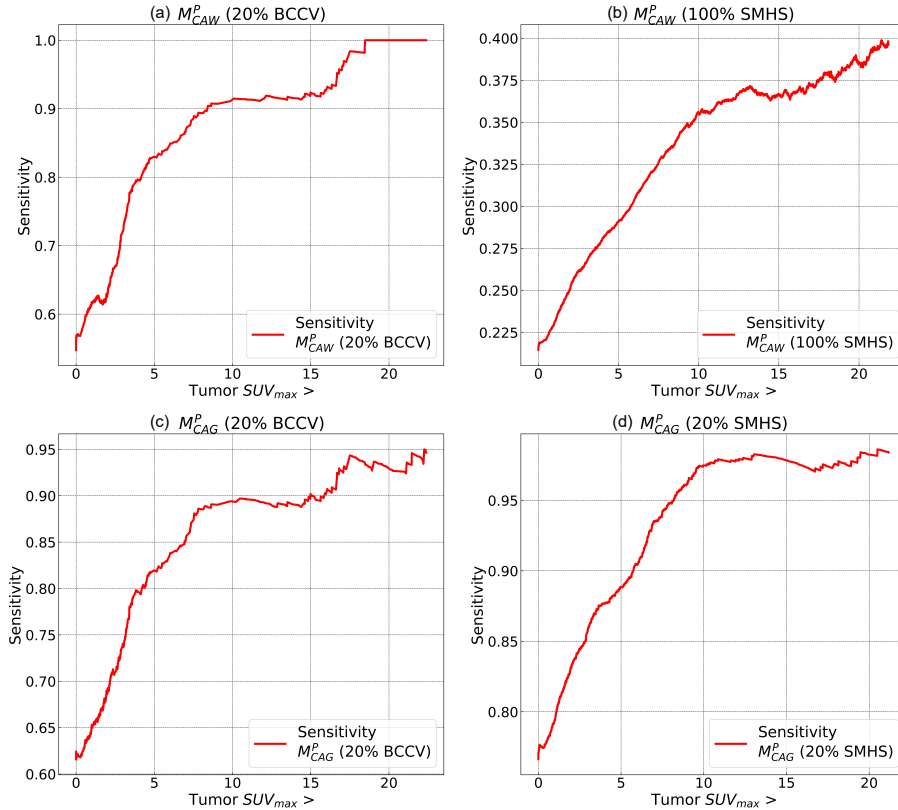


Figure 6. Sensitivity or true positive rate analysis as a function of tumor SUV_{\max} for the models (a) M_{CAW}^P (20% BCCV), (b) M_{CAW}^P (100% SMHS), (c) M_{CAG}^P (20% BCCV), and (d) M_{CAG}^P (20% SMHS) on their respective test sets (shown in brackets). Here, we unequivocally demonstrate that, as expected, there is an increase in sensitivity as a function of tumor $SUV_{\max} > u_i$, where u_i is the minimum tumor SUV_{\max} value among all the slices within the smaller test subset i (where $1 \leq i \leq [0.95m]$ and m is the total number of slices in the test set).

Finally, the positive slices in each of these test sets were arranged in increasing order of SUV_{\max} such that $u_1 \leq u_2 \leq \dots \leq u_{m-1} \leq u_m$, where u_i is the tumor SUV_{\max} value of the positive slice with the i^{th} largest SUV_{\max} and m is the total number of slices in the test set. Within each test set, different subsets of slices were chosen such that subset i consisted of all the slices with $SUV_{\max} \geq u_i$. Hence, the subset $i = 1$ consisted of all m slices, while the subset $i = m$ consisted of only the slice with $SUV_{\max} = u_m$. The sensitivity or true positive rate (= true positives/(total number of positives)) was computed on each of these subsets and plotted

as a function of u_i for $1 \leq i \leq \lfloor 0.95m \rfloor$, for each of M_{CAW}^P (20% BCCV), M_{CAW}^P (100% SMHS), M_{CAG}^P (20% BCCV), and M_{CAG}^P (20% SMHS), as shown in Figures 6(a), 6(b), 6(c), and 6(d), respectively. Each of these plots unequivocally shows that the percentage of correctly classified positive slices increases with an increase in tumor SUV_{\max} in the subset, showing that, as expected, the networks found it easier to correctly classify the positive slices containing tumors with higher SUV_{\max} .

4. DISCUSSION AND CONCLUSION

This study may also be extended by doing a similar analysis as in Figures 6(a)-6(d) for the negative slices, where the SUV_{\max} for a negative slice can be computed as the maximum non-tumorous SUV value within that slice. Furthermore, other classifiers with different pretrained backbone networks will be explored towards enhancing the classification performance further.

We trained different instances of a binary classifier neural network for the various train-test splits of the data and explored the model’s generalizability (via two training regimes, CAW and CAG) in the context of a multi-centric PET/CT dataset. We showed that the inclusion of CT slices provided no performance boost, at least for the models we trained with inputs containing a CT slice as the third channel. Further investigation into different CT preprocessing might be required to make the model efficiently use the rich anatomical information provided by the CT images.

We demonstrated unequivocally that the tumor SUV_{\max} on positive slices is important for the deep learning classifier to predict the class for positive slices. We also noted that the positive slices with larger tumor SUV_{\max} values are more likely to be classified correctly, as compared to the positive slices with lower tumor SUV_{\max} . It is worth noting that the tumor SUV_{\max} value is highly dependent on the PET reconstruction algorithms used. While this study did not consider the effects of different reconstruction algorithms used for different images from the two centers, this will be taken up as a separate study in future works.

ACKNOWLEDGEMENTS

This work was supported by the Canadian Institutes of Health Research (CIHR) Project Grant PJT-173231, the Mitacs Accelerate grant, and computational resources and services provided by Microsoft for Health.

REFERENCES

- [1] Slattery, A., “Validating an image segmentation program devised for staging lymphoma,” *Australas. Phys. Eng. Sci. Med.* **40**, 799–809 (Dec. 2017).
- [2] Weisman, A. J., Kim, J., Lee, I., McCarten, K. M., Kessel, S., Schwartz, C. L., Kelly, K. M., Jeraj, R., Cho, S. Y., and Bradshaw, T. J., “Automated quantification of baseline imaging PET metrics on FDG PET/CT images of pediatric hodgkin lymphoma patients,” *EJNMMI Phys.* **7**, 76 (Dec. 2020).
- [3] Ahamed, S., Dubljevic, N., Bloise, I., Gowdy, C., Martineau, P., Wilson, D., Uribe, C. F., Rahmim, A., and Yousefirizi, F., “A cascaded deep network for automated tumor detection and segmentation in clinical PET imaging of diffuse large B-cell lymphoma,” in *[Medical Imaging 2022: Image Processing]*, Colliot, O. and Išgum, I., eds., **12032**, 120323M, International Society for Optics and Photonics, SPIE (2022).
- [4] Capobianco, N., Meignan, M., Cottureau, A.-S., Vercellino, L., Sibille, L., Spottiswoode, B., Zuehlsdorff, S., Casasnovas, O., Thieblemont, C., and Buvat, I., “Deep-learning 18F-FDG uptake classification enables total metabolic tumor volume estimation in diffuse large b-cell lymphoma,” *J. Nucl. Med.* **62**, 30–36 (Jan. 2021).
- [5] Cottureau, A.-S., Versari, A., Loft, A., Casasnovas, O., Bellei, M., Ricci, R., Bardet, S., Castagnoli, A., Brice, P., Raemaekers, J., Deau, B., Fortpied, C., Raveloarivahy, T., Van Zele, E., Chartier, L., Vander Borgh, T., Federico, M., Hutchings, M., Ricardi, U., Andre, M., and Meignan, M., “Prognostic value of baseline metabolic tumor volume in early-stage hodgkin lymphoma in the standard arm of the H10 trial,” *Blood* **131**, 1456–1463 (Mar. 2018).

- [6] Blanc-Durand, P., Van Der Gucht, A., Schaefer, N., Itti, E., and Prior, J. O., “Automatic lesion detection and segmentation of 18F-FET PET in gliomas: A full 3D U-Net convolutional neural network study,” *PLoS One* **13**, e0195798 (Apr. 2018).
- [7] Ceriani, L., Milan, L., Martelli, M., Ferreri, A. J. M., Cascione, L., Zinzani, P. L., Di Rocco, A., Conconi, A., Stathis, A., Cavalli, F., Bellei, M., Cozens, K., Porro, E., Giovanella, L., Johnson, P. W., and Zucca, E., “Metabolic heterogeneity on baseline 18FDG-PET/CT scan is a predictor of outcome in primary mediastinal b-cell lymphoma,” *Blood* **132**, 179–186 (July 2018).
- [8] Ahamed, S., Toosi, A., Uribe, C., Rahmim, A., and Yousefirizi, F., “Towards enhanced automated tumor detection using background slice annotation methods in clinical pet imaging of lymphoma,” *Journal of Nuclear Medicine* **63**(supplement 2), 3346–3346 (2022).
- [9] Ahamed, S., Chaussé, G., Klyuzhin, I., Rahmim, A., and Yousefirizi, F., “A comparative study of tumor detection models trained on coronal versus sagittal versus axial pet imaging slices,” *Journal of Nuclear Medicine* **63**(supplement 2), 3245–3245 (2022).
- [10] Zhao, X., Li, L., Lu, W., and Tan, S., “Tumor co-segmentation in PET/CT using multi-modality fully convolutional neural network,” *Phys. Med. Biol.* **64**, 015011 (Dec. 2018).
- [11] Shen, D., Wu, G., and Suk, H.-I., “Deep learning in medical image analysis,” *Annual Review of Biomedical Engineering* **19**(1), 221–248 (2017). PMID: 28301734.
- [12] Haenssle, H. A., Fink, C., Schneiderbauer, R., Toberer, F., Buhl, T., Blum, A., Kalloo, A., Hassen, A. B. H., Thomas, L., Enk, A., Uhlmann, L., Reader study level-I and level-II Groups, Alt, C., Arenbergerova, M., Bakos, R., Baltzer, A., Bertlich, I., Blum, A., Bokor-Billmann, T., Bowling, J., Braghiroli, N., Braun, R., Buder-Bakhaya, K., Buhl, T., Cabo, H., Cabrijan, L., Cevic, N., Classen, A., Deltgen, D., Fink, C., Georgieva, I., Hakim-Meibodi, L.-E., Hanner, S., Hartmann, F., Hartmann, J., Haus, G., Hoxha, E., Karls, R., Koga, H., Kreuzsch, J., Lallas, A., Majenka, P., Marghoob, A., Massone, C., Mekokishvili, L., Mestel, D., Meyer, V., Neuberger, A., Nielsen, K., Oliviero, M., Pampena, R., Paoli, J., Pawlik, E., Rao, B., Rendon, A., Russo, T., Sadek, A., Samhaber, K., Schneiderbauer, R., Schweizer, A., Toberer, F., Trennheuser, L., Vlahova, L., Wald, A., Winkler, J., Wölbing, P., and Zalaudek, I., “Man against machine: diagnostic performance of a deep learning convolutional neural network for dermoscopic melanoma recognition in comparison to 58 dermatologists,” *Ann. Oncol.* **29**, 1836–1842 (Aug. 2018).
- [13] Ardila, D., Kiraly, A. P., Bharadwaj, S., Choi, B., Reicher, J. J., Peng, L., Tse, D., Etemadi, M., Ye, W., Corrado, G., Naidich, D. P., and Shetty, S., “End-to-end lung cancer screening with three-dimensional deep learning on low-dose chest computed tomography,” *Nat. Med.* **25**, 954–961 (June 2019).
- [14] Wu, N., Phang, J., Park, J., Shen, Y., Huang, Z., Zorin, M., Jastrzebski, S., Fevry, T., Katsnelson, J., Kim, E., Wolfson, S., Parikh, U., Gaddam, S., Lin, L. L. Y., Ho, K., Weinstein, J. D., Reig, B., Gao, Y., Toth, H., Pysarenko, K., Lewin, A., Lee, J., Airola, K., Memma, E., Chung, S., Hwang, E., Samreen, N., Kim, S. G., Heacock, L., Moy, L., Cho, K., and Geras, K. J., “Deep neural networks improve radiologists’ performance in breast cancer screening,” *IEEE Trans. Med. Imaging* **39**, 1184–1194 (Apr. 2020).
- [15] Yousefirizi, F., Dubljevic, N., Ahamed, S., Bloise, I., Gowdy, C., O, J. H., Farag, Y., de Schaetzen, R., Martineau, P., Wilson, D., Uribe, C. F., and Rahmim, A., “Convolutional neural network with a hybrid loss function for fully automated segmentation of lymphoma lesions in FDG PET images,” in [*Medical Imaging 2022: Image Processing*], Colliot, O. and Išgum, I., eds., **12032**, 120320V, International Society for Optics and Photonics, SPIE (2022).
- [16] Warfield, S. K., Zou, K. H., and Wells, W. M., “Simultaneous truth and performance level estimation (STAPLE): an algorithm for the validation of image segmentation,” *IEEE Trans. Med. Imaging* **23**, 903–921 (July 2004).
- [17] Lev, M. and Gonzalez, R., “17 - ct angiography and ct perfusion imaging,” in [*Brain Mapping: The Methods (Second Edition)*], Toga, A. W. and Mazziotta, J. C., eds., 427–484, Academic Press, San Diego, second edition ed. (2002).
- [18] He, K., Zhang, X., Ren, S., and Sun, J., “Deep residual learning for image recognition,” (2015).
- [19] Lin, T.-Y., Goyal, P., Girshick, R., He, K., and Dollár, P., “Focal loss for dense object detection,” (2017).